



Two-dimensional and multi-channel feature detection algorithm for the CALIPSO lidar measurements

Thibault Vaillant de Guélis^{1,2}, Mark A. Vaughan³, David M. Winker³, and Zhaoyan Liu³

¹NASA Postdoctoral Program Fellow, NASA, Langley Research Center, Hampton, VA 23681, USA

²Science Systems and Applications, Inc., Hampton, VA 23666, USA

³NASA Langley Research Center, Hampton, VA 23681, USA

Correspondence: Thibault Vaillant de Guélis (thibault.vaillantdeguelis@outlook.com)

Abstract. In this paper we describe a new two-dimensional and multi-channel feature detection algorithm (2D-McDA) and demonstrate its application to lidar backscatter measurements from the Cloud-Aerosol Lidar and Infrared Pathfinder Satellite Observations (CALIPSO) mission. Unlike previous layer detection schemes, this context sensitive feature finder algorithm is applied to a 2D lidar "scene"; i.e., to the image formed by many successive lidar profiles. Features are identified when an extended and contiguous 2D region of enhanced backscatter signal rises significantly above the expected "clear air" value. Using an iterated 2D feature detection algorithm dramatically improves the fine details of feature shapes and can accurately identify previously undetected layers (e.g., subvisible cirrus) that are very thin vertically but horizontally persistent. Because the algorithm looks for consistent 2D patterns, it potentially offers improved discrimination of juxtaposed cloud and aerosol layers. Moreover, the 2D detection algorithm uses the backscatter signals from all available channels: 532 nm parallel, 532 nm perpendicular, and 1064 nm total. Since the backscatter from some aerosol or cloud particle types can be more pronounced in one channel than another, simultaneously assessing the signals from all channels greatly improves the layer detection. For example, ice particles in subvisible cirrus strongly depolarize the lidar signal and, consequently, are easier to detect in the 532 nm perpendicular channel. Use of the 1064 nm channel greatly improves the detection of dense smoke layers, because smoke extinction at 532 nm is much larger than at 1064 nm, and hence the range-dependent reduction in lidar signals due to attenuation occurs much faster at 532 nm than at 1064 nm. Moreover, the photomultiplier tubes used at 532 nm are known to generate artifacts in an extended area below highly reflective liquid clouds, introducing false detections that artificially lower the apparent cloud base altitude, i.e. the cloud base when the cloud is transparent or the level of complete attenuation of the lidar signal when it is opaque. By adding the information available in the 1064 nm channel, this new algorithm can better identify the true apparent cloud base altitudes of such clouds.

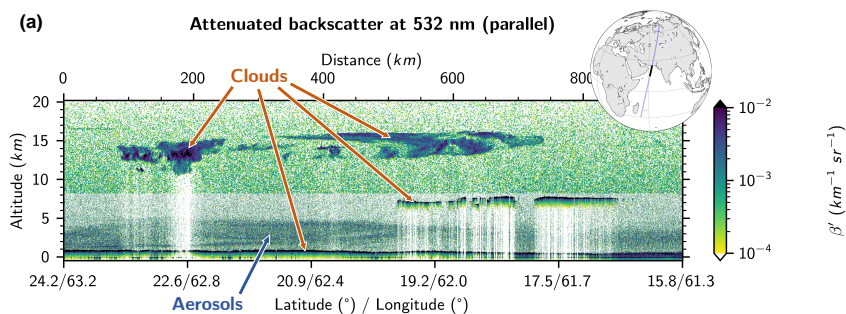


Figure 1. Curtain of lidar attenuated backscatter signal measured by CALIOP in the 532 nm parallel channel during nighttime observations on August 31, 2018, 21:46:37 UTC (start point), over Arabian Sea.

1 Introduction

The Cloud–Aerosol Lidar and Infrared Pathfinder Satellite Observation (CALIPSO) mission (Winker et al., 2010) has provided direct measurements of cloud and aerosol vertical distributions with a very high vertical resolution since 2006. A key component of these measurements is made by the active remote sensing instrument CALIOP (i.e., the Cloud-Aerosol Lidar with Orthogonal Polarization), a two-wavelength (532 nm and 1064 nm), polarization sensitive elastic backscatter lidar.

The knowledge of the cloud and aerosol vertical distributions and their properties is critical in assessing the planet’s radiation budget (e.g., Shonk and Hogan, 2010), in evaluating the atmospheric radiative heating rate (e.g., Huang et al., 2009), and for advancing our understanding of cloud-climate feedback cycles that occur as the climate warms (e.g., Tsushima et al., 2006).

The critically important first step in retrieving the spatial and optical properties of clouds and aerosols is to determine where these "features" are located in the vertical, curtain-like images (altitude vs. satellite track) of the backscattered lidar signals (Fig. 1). The CALIPSO feature detection algorithms were first developed for ground-based observations, and then adapted for space-based analyses using LITE measurements and CALIPSO simulations. These algorithms, which were conceived more than 25 years ago (e.g., Winker and Vaughan, 1994), at a time when computational power was considerably less than is now available, are invoked sequentially on single, one-dimensional (1D) lidar signal profiles (possibly generated from averaging data from several consecutive laser pulses). Moreover, in order to minimize the computational load, the current CALIPSO algorithm is only applied to the 532 nm total signal (Vaughan et al., 2009).

To locate cloud and aerosol layers within lidar backscatter profiles, two main approaches are generally employed: the slope-based method, which looks for zero crossings in the first derivative of the raw signal (e.g., Pal et al., 1992) and threshold-based methods, which search for regions exceeding some expectation of the maximum signal value that could be measured in "clear air" (e.g., Winker and Vaughan, 1994; Clothiaux et al., 1998; Campbell et al., 2008). Some studies use a combination of both methods (e.g., Wang and Sassen, 2001; Lewis et al., 2016). A few others adopt a third method: the wavelet analysis (e.g., Davis et al., 2000; Brooks, 2003). All these methods are *profile processes*: the detection algorithm is applied to individual (or averaged) 1D profiles. Another appealing class of methods are known as *scene processes*. These methods can take advantage of



the contextual information provided by a continuous series of profile measurements by searching for cloud and aerosol patterns
 45 in the two-dimensional (2D) image formed by successive lidar profiles. If edge detection techniques based on 2D gradient
 search routines do not seem adequate for spatial analysis of lidar data (Vaughan et al., 2005), methods based on sliding window
 operations have shown to greatly improves the feature shape detection (e.g., Hagihara et al., 2010; van Zadelhoff et al., 2011;
 Herzfeld et al., 2014).

Here we propose a new 2D and multi-channel feature detection algorithm (2D-McDA). This "context sensitive" feature finder
 50 algorithm is then applied to a 2D lidar signal scene; i.e., to the image formed by many successive lidar profiles. Moreover, the
 2D detection algorithm uses the backscatter signals from all available channels: the 532 nm co-polarized (or parallel) signal,
 the 532 nm cross-polarized (or perpendicular) signal, and the 1064 nm signal. Since the backscatter from some aerosol or cloud
 particle types can be more pronounced in one channel than another, simultaneously assessing the signals from all channels is
 expected to greatly improve the layer detection.

Section 2 presents a refined method for determining feature detection thresholds, which are a critically important component
 55 of the detection algorithm. Section 3 presents the detection algorithm. The detection of the Earth's surface is described first as it
 is performed first and separately from the cloud and aerosol detection. This has been shown to have many practical advantages.
 Then, the cloud and aerosol detection algorithm is described. Finally, the detections from each channel are merged into a
 composite feature detection mask. Section 4 shows how this new algorithm improves the feature detection compared to the
 60 CALIPSO version 4 vertical feature mask (VFM).

2 Threshold based feature detection

Atmospheric lidars measure attenuated signal backscattered by molecules (m) and particles (p)

$$\beta'(r) = (\beta_m(r) + \beta_p(r))T_m(r)^2T_{O_3}(r)^2T_p(r)^2, \quad (1)$$

where $\beta_m(r)$ and $\beta_p(r)$ are the volume backscatter coefficients for molecules and particulates, and $T_m(r)^2$, $T_{O_3}(r)^2$ and
 65 $T_p(r)^2$ are, respectively, the two-way transmittances for molecules, ozone, and particles, and r is the range from the satellite
 altitude. If there are no particles in the atmosphere, Eq. (1) reduces to the molecular attenuated backscatter coefficient

$$\beta'_m(r) = \beta_m(r)T_m(r)^2T_{O_3}(r)^2. \quad (2)$$

A feature, i.e., a cloud or an aerosol layer, appears as an extended and contiguous region of enhanced attenuated backscatter
 signal that rises significantly above the expected clear sky (molecules only) value. To detect these features, a first step is to
 70 determine a threshold above which the attenuated backscatter signal should be considered as due to an atmospheric feature. Not
 all signals larger than the expected molecular attenuated backscatter signal $\widehat{\beta'_m(r)}$ are necessarily due to real features; instead
 they can be caused by noise. A range-dependent threshold is computed following

$$\beta'_T(r) = \widehat{\beta'_m(r)} + k \frac{f_{\text{corr}}(r)}{\sqrt{N(r)}} \sqrt{\Delta\beta'_b(r)^2 + \Delta\beta'_m(r)^2}, \quad (3)$$

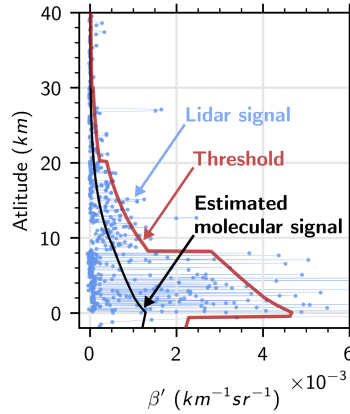


Figure 2. Range-dependent threshold (red) applied to a single shot lidar signal profile (blue) in clear-sky during nighttime. The estimated molecular signal is shown in black.

where $\Delta\beta'_b(r)$ is the standard deviation due to background noise (range-independent¹), $\widehat{\Delta\beta'_m(r)}$ is the expected standard deviation due to the shot noise (range-dependent) in the expected clear sky, and $N(r)$ is the number of bins averaged. The $f_{\text{corr}}(r)$ term is a correction function which takes into account the partial vertical correlation in samples due to the limited electronic bandwidth and the shifting and rebinning that can occur in the altitude registration phase of the level 1A processing (details in Appendix A). The number of shot noise standard deviations considered in the threshold is quantified by the factor k , which can be tuned according to the degree of sensitivity needed to avoid false detections. $\widehat{\beta'_m(r)}$ is derived from modeled profiles of molecular and ozone number densities. $\Delta\beta'_b(r)$ is derived from the on-board computation of the root mean square (RMS) of the background signal in the high altitude background region (HABR) between 65 and 80 km for each shot (Hostetler et al., 2006). $\widehat{\Delta\beta'_m(r)}$ is estimated using its proportional relation with the square root of $\widehat{\beta'_m(r)}$ (e.g., Liu and Sugimoto, 2002), called *noise scale factor* (NSF)

$$\widehat{\Delta\beta'_m(r)} = NSF_{\beta'} \sqrt{\widehat{\beta'_m(r)}}. \quad (4)$$

The NSF is evaluated from the solar background signal during daytime for the 532 nm parallel and perpendicular channels (Hostetler et al., 2006; Liu et al., 2006). At 1064 nm, CALIOP uses an avalanche photodiode (APD) detector, rather than the photomultiplier tubes (PMTs) that are used for the 532 nm channels. Because the APD dark noise overwhelms the 1064 nm shot noise, only the background noise is considered at 1064 nm.

Figure 2 shows the range-dependent threshold (red) computed from Eq. (3) with $k = 2$ applied to the 532 nm parallel lidar signal (blue) for a clear-sky case study during nighttime. Note the noise due to the quantum nature of photons (shot-noise) in this figure. Indeed, although background noise, mainly due to solar radiation, is quite low during nighttime, the lidar signal shows large variations around the expected clear-sky return (black). The range-dependent threshold correctly keeps most the signal below the detection level. Jumps at 8.2 and 20.2 km reveal the change of onboard averaging resolution. However, a

¹The background noise is range-independent in the digitizer-reading domain P . However, it then depends on r when transformed to the β' domain.

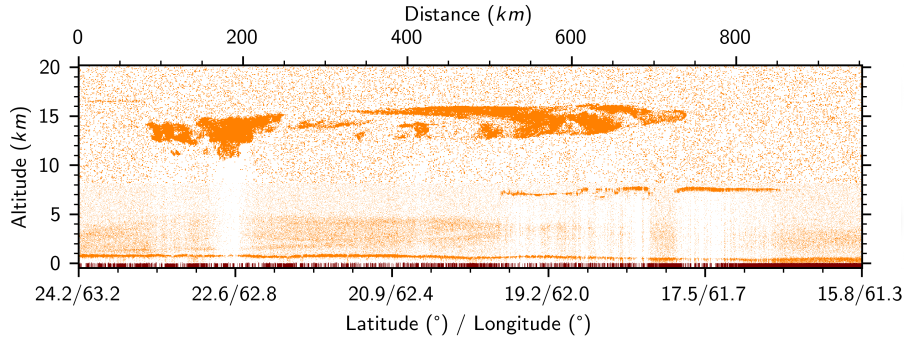


Figure 3. Pixels of Fig. 1 where the lidar signal is above the range-dependent threshold computed from Eq. (3) with $k = 2$ are shown in orange. Brown pixels show surface detection.

few points of the lidar signal still exceed the threshold. Some continuity tests are then needed to determine whether these high
 95 signals are due to noise or instead part of an extended feature. Unlike the current CALIPSO detection algorithm, this continuity
 test will be applied in two dimensions. Figure 3 shows all pixels of Fig. 1 where the lidar signal is above the range-dependent
 threshold computed from Eq. (3) with $k = 2$.

For practical reasons, the layer detection scheme uses the attenuated scattering ratio

$$R'(r) = \frac{\beta'(r)}{\beta'_m(r)} \quad (5)$$

100 rather than the attenuated backscatter. The attenuated scattering ratio threshold is then obtained from

$$R'_T(r) = \frac{\beta'_T(r)}{\beta'_m(r)} = 1 + k \frac{f_{\text{corr}}(r)}{\sqrt{N(r)}} \sqrt{\frac{1}{\beta'_m(r)^2} \Delta\beta'_b(r)^2 + NSF_{\beta'}^2 \frac{1}{\beta'_m(r)}}. \quad (6)$$

Equation (6) is applied to the three lidar channels (532 nm parallel, 532 nm perpendicular, and 1064 nm) during the 2D-McDA process.

3 2D and multi-channel feature detection algorithm

105 2D-McDA is applied to the scattering ratio signals at 532 nm parallel, 532 nm perpendicular, and 1064 nm. First, the detection
 of the surface altitude is performed and the signal from this altitude and below is removed from the data. Second, the detection
 of cloud and aerosol layers is done in each channel based on iterated detection thresholds and 2D spatial continuity tests.
 Finally, the masks from the three channels are merged in a composite feature mask.



3.1 Surface detection

110 Before detecting cloud and aerosol layers using the detection threshold as described in the previous section, we perform first
an independent surface detection. Doing the surface detection in a first and separate step allows a better retrieval of the surface
echo and prevents complications in the cloud and aerosol layer detection process. Also, knowing where the surface is detected
allows subsequent separation of *semi-transparent* features from *opaque* features, which is essential for accurately estimating
range-resolved profiles of extinction coefficients (Young et al., 2018). Operationally, atmospheric features are defined as being
115 opaque when no surface return or other atmospheric feature can be detected below them. From this definition it follows that the
signals received from beneath opaque features have been fully attenuated within these features. The surface detection algorithm
used here is closely akin to the one described in Vaughan et al. (in progress) and is applied to the 532 nm parallel and 1064 nm
channels (details in Appendix B). The signals from the top of the detected surface echo and below this point are removed from
the data. To minimize computation times, the surface detection algorithm is not applied to the 532 nm perpendicular channel
120 signal. The backscatter from ocean surfaces (covering ~70% of the planet) does not depolarize and, excluding snow and ice, the
depolarization of most land surfaces is relatively low (Lu et al., 2017), hence the preponderance of the surface backscatter is in
the parallel channel. The altitude retrieved in the parallel channel is used to remove signal at and below the estimated surface
altitude in the perpendicular channel. Note that there is some small chance that a surface echo can appear in the perpendicular
channel but not be visible/detected in the parallel channel. The detection of the surface corresponding to Fig. 1 is shown in
125 brown on Fig. 3.

3.2 Cloud and aerosol detection

The detection of cloud and aerosol layers in a single channel curtain of lidar measurements takes place in four main steps:

1. Detecting strong features; i.e., identifying contiguous regions of enhanced attenuated scattering ratios that rise above the
feature detection threshold (which is repeatedly decreased from very large value of k down to $k = 1$) without applying
130 any signal averaging (i.e., $d = 1 - 4$ in Table 1, refer to Sect. 3.2.1);
2. Flagging regions below opaque features as “fully attenuated” (FA) and regions below transparent features where the
signal is strongly attenuated with the low confidence flag “almost fully attenuated” (AFA) (Sect. 3.2.2);
3. Averaging of those signals not already flagged using a horizontal sliding window (Sect. 3.2.3);
4. Detecting faint features; features are once again identified as contiguous regions of enhanced signal (i.e., averaged
135 attenuated scattering ratios) that rise above the recomputed feature detection threshold (Sect. 3.2.1).

Figure 4 shows the flowchart of the whole detection algorithm. The parameter values used at the different detection levels
are given in Table 1.

The following subsections give the details of the main steps presented above.

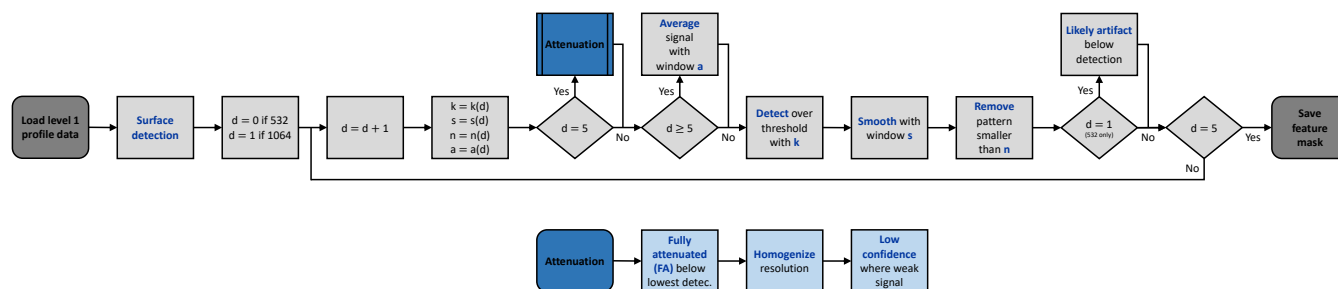


Figure 4. Flowchart of the two-dimensional and multi-channel feature detection algorithm (2D-McDA).

3.2.1 Detection

140 The detection phase is performed following three substeps:

1. All pixels of within image that exceed the threshold are first flagged as detected (Fig. 3);
2. A spatial coherence test window is applied to the image of detected/undetected pixels. It smooths the shape of detected pattern and remove isolated noisy detected pixels by turning some of detected pixels to undetected or undetected to detected;
- 145 3. Smoothed patterns are required to meet a minimum numeric threshold of contiguous pixels. Patterns that fail to meet this threshold are removed from consideration for this level of detection.

The scattering ratio image used in the layer detection scheme has a spatial resolution of one laser pulse horizontally and 30 m vertically, equivalent to the finest spatial resolution of the CALIOP data. As described in Hunt et al. (2009), CALIOP data is averaged onboard the satellite with spatial resolutions that vary according to altitude. Scattering ratios in regions where the data resolution is coarser than the image resolution are duplicated to the image resolution. The first substep is then to flag all pixels of this image which exceed the detection threshold given by Eq. (6) with the value of k defined in Table 1. For example, for the 532 nm parallel channel, at the detection level $d = 3$, the detected pixels are those where signal is greater than $1 + k$ times the expected noise standard deviation with $k = 2$ (Fig. 5a; orange pixels). Then, the second substep is to apply a spatial coherence test window (rows a in Table 1) on these detected pixels (Fig. 5a,b). Here, an 11×11 pixels window is applied to each pixel of the image, with the window being centered successively on all pixels. If the number of originally detected pixels in the window is greater than half of the total number of pixel in the window (≥ 61 for a 11×11 pixels window), then the center pixel is considered as detected. If not, the center pixel is considered as not detected. In this smoothing step, the determination of detection status does not rely on a single pixel exceeding its threshold, but instead on the fraction of neighboring pixels that exceed their thresholds. Consequently, a pixel classified as detected may not itself exceed the detection threshold. Similarly, a pixel that exceeds the threshold may not ultimately be classified as detected. The pixel count within the window is limited to those detected at the current detection level d and at the previous detection level $d - 1$. This allows detection continuity of



Table 1. Coefficient **k** in threshold detection, spatial coherence test window size **s**, minimum number of pixels in pattern **n**, and averaging window size **a** used at each detection step **d**. Window sizes are given in vertical \times horizontal in pixel number with pixel resolution of 30 m \times 0.33 km.

d	1	2	3	4	5	
532 nm parallel	k	100	20	2	1	1
	s	–	–	11 \times 11 (330 m \times 3.67 km)	3 \times 21 (90 m \times 7 km)	9 \times 51 (270 m \times 17 km)
	n	1	1	60	200	10000
	a	–	–	–	–	1 \times 15 (30 m \times 5 km)
532 nm perpendicular	k	500	100	2	1	1
	s	–	–	11 \times 11 (330 m \times 3.67 km)	3 \times 21 (90 m \times 7 km)	9 \times 51 (270 m \times 17 km)
	n	1	1	60	200	1000
	a	–	–	–	–	1 \times 15 (30 m \times 5 km)
1064 nm	k	–	20	2	1	1
	s	–	–	11 \times 11 (330 m \times 3.67 km)	3 \times 21 (90 m \times 7 km)	9 \times 51 (270 m \times 17 km)
	n	–	1	60	200	10000
	a	–	–	–	–	1 \times 15 (30 m \times 5 km)

similar backscatter intensities and avoids connecting noise encountered during fainter detections to a strong feature detected earlier. Other flagged pixels (i.e., "Surface", detection $\leq d - 2$, "Likely artifact", "Fully attenuated", "Almost fully attenuated", and "Low confidence small strips" (to be described in detail later in this subsection and subsection 3.2.2)) are not considered in the window and the total number of candidate pixels in the window is decreased accordingly. The shapes of detected features are smoothed by the spatial coherence test window, while the noise (isolated orange pixel) is removed. However, some small clusters of pixels sometimes persist. Those small clusters cannot be confidently declared as feature at this stage. They can be due to noise or they can be part of a larger, fainter feature. Then, we decide not to consider these small patterns as detected feature

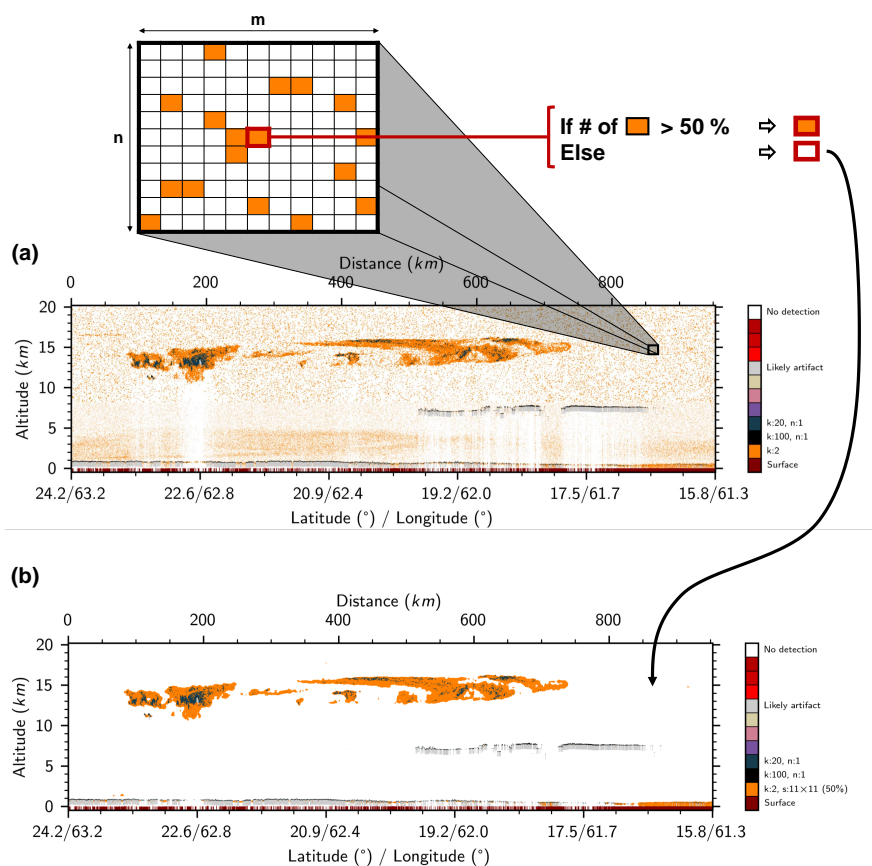


Figure 5. Illustration of the spatial coherence test window substep of 2D-McDA on the 532 nm parallel channel for the case study shown in Fig. 1. (a) Pixels which are over the detection threshold given by Eq. (6) with the value of $k = 2$ (orange). (b) Result after applying a 11×11 spatial coherence test window on the detected pixels. Note that the insert on the top is just an illustration and does not show the real content of the image portion.

and retain these regions for inclusion in the signal averaging used in successive iterations of the algorithm. To be declared as
 170 detected feature, smoothed detected patterns need to consist of more than n connected pixels (see Table 1), otherwise they are
 removed from this detection level.

This detection procedure is applied several times with different thresholds, different spatial coherence test window, and
 different limits on the number of connected pixels required (Table 1) in order to detect all layers from the most evident, very
 strong patterns to the very faint ones, and from geometrically small patterns to very extended ones. Note that the horizontal
 175 spatial coherence test window (3×21) enables the detection of faint but horizontally extended cirrus such as the layer shown
 between 50 km and 100 km in Fig. 1. The detection of this subvisible cirrus is presented in Fig. 6. Figure 6a to Fig. 6b shows
 the implementation of the 3×21 spatial coherence test window. We see that the cirrus pattern is smoothed and now clearly



appears on Fig. 6b due to the fact that most of the noise around has been removed. However, many small clusters of pixels
persist. By applying the minimum numeric threshold on the detected pattern, we are able to remove small cluster due to noise
180 while keeping the real cirrus (Fig. 6c).

3.2.2 Special flags

For the 532 nm channels, a first detection of very strong signal is performed (see $d = 1$ in Table 1). The aim of this initial scan
is to identify the tops of very strongly scattering liquid clouds and ice clouds containing high fractions of horizontally oriented
ice (HOI) crystals. The non-ideal transient response by PMTs following these very strong signals often generates a spurious,
185 exponentially decaying signal enhancement in the underlying range bins (McGill et al., 2007; Hunt et al., 2009; Lu et al., 2020).
The presence of these "noise tails" in the 532 nm signals can introduce large biases into the determination of the apparent bases
of opaque water clouds. To exclude this artifact in the detection process, the 600 m below the base of the detected very strong
signal are flagged as "Likely artifact" and removed from the signal. Since the APD used in 1064 nm channel does not produce
these noise tails, we rely on the 1064 nm channel for the detection of the apparent base of these strongly scattering layers.

190 After detection of the strongest features, i.e without signal averaging ($d = 1 - 4$ in Table 1), we flag as "Fully attenuated"
(FA) all pixels below a detected strong feature where the surface has not been detected. In this portion of the profile, the signal
is too weak to be further exploited. Second, pixels where the signal is considered possibly too weak are flagged as "Almost
fully attenuated" (AFA). Pixels flagged as AFA are those vertically between two detected features if more than 30 % of them
have their signal less than 10 % of the threshold for the 532 nm parallel channel, or more than 90 % and 85 % of them have
195 their signal less than the threshold for the 532 nm perpendicular and 1064 nm channel respectively. These thresholds have been
found experimentally and are tunable. Finally, the horizontal distance between successive (A)FA columns can be very small
and any attempt to detect something here with the 2D-McDA algorithm aims to some issues. Then, the data in all horizontal
spaces between (A)FA columns smaller than 5 km (15 profiles) are flagged as "Low confidence small strips".

200 After removing all data identified with these low confidence flags from the attenuated scattering ratios, the signal is averaged
in order to try to detect fainter features.

3.2.3 Signal averaging

We then average the remaining signal (here the attenuated scattering ratios) using an edge-preserving Gaussian sliding window
that extends over 5 km (15 profiles) horizontally and a single range bin vertically (a in Table 1). A Gaussian weight with a
standard deviation of 1.67 km is applied, thus giving a stronger weight to pixels closer to center of the window than at the
205 edges. We chose a horizontal window here because the spatial extent of very faint layers is mainly in the horizontal direction.
Once the averaging is performed, the detection substeps (Sect. 3.2.1) are then applied to the averaged signal. Note that any
feature split by a low confidence vertical band (FA, AFA, and small strips) is considered as a unique feature when counting the
number of connected pixels.

Figure 7 shows the final mask for the 532 nm parallel channel after the detection of the faint features.



210 3.3 Three channels composite detection

The detection algorithm is applied individually to the lidar signal from each of the three channels (Fig. 8) and all pixels identified as features in any of the three channels are retained in the composite mask (Fig. 9a). Comparing this new feature mask (Fig. 9a,b) to the current version of the Vertical Feature Mask (VFM) (Fig. 9c), we first note the improvement in the detected contour of the large cirrus. We also note that the 2D-McDA readily detects faint cirrus (e.g., as seen between 0 km and 215 75 km) that is missed by the current VFM. The vertical spreading of the clouds seen in the VFM at around 7.5 km in altitude and between 500 km and 900 km horizontally is due to the aforementioned PMT artifact afflicting the 532 nm signals beneath strongly scattering layers. This is not seen in the 2D-McDA feature mask because pixels below the cloud top are flagged as "Likely artifact" in the 532 nm channels and so we make no attempt to retrieve the cloud apparent base of such opaque clouds at this wavelength. Instead, in these cases we retrieve the true penetration depth estimates using the 1064 nm signals (Fig. 8c), 220 which are not affected by detector transient response artifacts (see light blue = "1064 only").

4 Performance assessments and comparisons to version 4

In this section, we present two case studies to show the improvements bring by this new feature detection approach.

4.1 Dense smoke

Figure 10 presents a dense smoke event in Siberia on July 26, 2006 during daytime. The smoke layer is opaque at 532 nm and thus we do not see any surface echo for this channel (Fig. 10a). Note that the smoke is non-depolarizing so there is no perpendicular signal (Fig. 10b). Because the standard CALIOP layer detection only examines the 532 nm channel, the VFM (Fig. 11c) indicates that the signals are fully attenuated after detecting (at 532 nm) the apparent base of the smoke layer. However, at 1064 nm the dense smoke layer is transparent and the surface is readily detected (Fig. 10c). This scene clearly illustrates the advantage gained by using a multi-channel feature detection algorithm, since the full vertical extent of the smoke 230 plume can only be retrieved by inspecting the 1064 nm measurements (light blue in Fig. 11a).

4.2 Variety of cloud type and shape

Figure 12 presents the attenuated backscattered lidar signal in the three channels for another case study showing a variety of cloud types and shapes which occurred above Ethiopia on August 31, 2018 during nighttime. We can see that the artifacts below liquid water clouds (close to the surface and up to 8 km) appear in the 532 nm parallel (Fig. 12a) and the 532 nm perpendicular (Fig. 12b) channels but not at 1064 nm (Fig. 12c). We note that thin cirrus clouds, like the one at 17 km in altitude between 1550 km and 1850 km, are clearly brought out in the 532 nm perpendicular channel (Fig. 12b). If we look now at the composite feature detections derived from these three signals (Fig. 13a), we note again how well the apparent bases of liquid clouds are retrieved by using the 1064 nm channel. We note also that the successful identification of thin cirrus can largely be attributed to our use of the 532 nm perpendicular channel. Figure 13b shows the same mask as Fig. 13a but with the same colors that are



240 used for the VFM images (Fig. 13c). This change of colors is intended to facilitate one-to-one comparisons between the two
detection schemes. However, note that the yellow and white colors do not discriminate aerosol from cloud, as in the VFM, but
instead simply differentiate weak from strong features based on whether the feature detection required data averaging (yellow)
or not (white). Finally, Figure 13d shows the difference between the new composite feature detection mask and the VFM.
We see that the contour of features retrieved by the 2D-McDA represents a distinct improvement over the squared boundaries
245 reported by the VFM. We note too that the new algorithm detects thin clouds that are obviously missed by the VFM and that it
eliminates significant detection artifacts reported by the VFM between 700 km and 900 km.

5 Conclusions

This paper describes the architecture and theoretical underpinnings of a new two-dimensional, multi-channel feature detection
algorithm (2D-McDA) used to identify layer boundaries in the backscatter signals acquired by the elastic backscatter lidar
250 aboard the Cloud Aerosol Lidar and Infrared Pathfinder Satellite Observations (CALIPSO) platform. The layer detection
algorithms used to generate the standard CALIPSO data products retrieve cloud and aerosol layer boundaries by scanning
sequences of individual lidar profiles constructed at varying horizontal averaging resolutions. In contrast, the 2D-McDA is
more akin to an image processing algorithm that examines full resolution lidar scenes and hence can identify many of the fine
details that are often obscured by CALIPSO's standard multi-resolution averaging scheme. Relative to the CALIPSO version
255 4.2 vertical feature mask (VFM) data product, the 2D-McDA shows the following improvements.

- Because it is applied to single profiles averaged over several different horizontal resolutions, the standard CALIOP fea-
ture detection produces blocky, rectangular layers. The complex shapes of aerosol and cloud features are better preserved
by the 2D-McDA windowing and data aggregation operations, which provide the flexibility required to distinguish fine
spatial details. It is hoped that this improved feature detection will lead to improvements in classifying features according
260 to type (e.g., clouds vs. aerosols) and in their optical property retrievals. Ideally, it will also offer improved discrimination
between juxtaposed cloud and aerosol layers or identifiable regions of ice and liquid water in a cloud. The improvement
of the cloud shape detection is by itself important for example for studies interested in anvil clouds (e.g., Bony et al.,
2016; Hartmann, 2016);
- The detection of subvisible cirrus is significantly enhanced by both the 2D detection scheme and the use of the 532 nm
265 perpendicular channel, which is especially sensitive to the presence of depolarizing ice crystals. Those clouds play an im-
portant role in the climate system as they regulate the vertical transport of water vapor near the upper troposphere–lower
stratosphere (e.g., Jensen et al., 1996; Luo et al., 2003), influence the local thermal budget, and drive dynamics of the
tropopause region (e.g., Hartmann et al., 2001; McFarquhar et al., 2000);
- The apparent base altitudes of highly reflective clouds, i.e. the levels of complete attenuation of the lidar signal, which are
270 routinely biased low (by several hundred meters) due to the non-ideal transient response of 532 nm photomultiplier tubes,
are now more correctly retrieved by incorporating measurements made by the 1064 nm channel. This altitude level has



been directly linked with the amount of longwave radiation escaping the Earth at the top of the atmosphere (Vaillant de Guélis et al., 2017a, b), making its accurate estimation very important for cloud feedback studies (Vaillant de Guélis et al., 2018);

- 275 – The 2D-McDA can retrieve the full vertical extent of dense smoke layers by examining the 1064 nm channel. Within
 smokes, the 1064 nm signals are attenuated significantly less than at 532 nm and hence can generally penetrate the full
 vertical extent of these layers. Those biomass burning aerosols play a significant role in the Earth’s radiative balance
 by their scattering and absorption of incoming solar radiation (e.g., Penner et al., 1992; Christopher et al., 1996) and
 the interaction they have with clouds (e.g., Kaufman and Fraser, 1997). The full detection of those layers will lead to
 280 more accurate aerosol optical depth retrievals, which will improve estimates of the radiation budget and interactions with
 clouds.

While the current implementation of the algorithm is computationally intensive, numerous optimizations are underway, and
 it is now feasible to apply the 2D-McDA operationally using CALIPSO’s available computer resources. However, taking full
 advantage of the new algorithm requires development of a companion set of scene classification algorithms that, similar to the
 285 2D-McDA, evaluate the feature type of 2D regions within lidar scenes, rather than on the layer-by-layer basis implemented in
 the current generation of CALIPSO algorithms.

Data availability. The CALIPSO level 1 lidar profile product are available at: doi.org/10.5067/CALIOP/CALIPSO/LID_L1-Standard-V4-10,
 last access: 3 September 2020.

Appendix A: Correction functions

290 A1 Correction due to electronic bandwidth

A 15-m bin b_i has a variance $\text{Var}(b_i)$. If N_{bin} 15-m bins are vertically averaged together to form a larger bin B , then the
 variance of the mean is given by

$$\begin{aligned} \text{Var}(B) &= \text{Var}\left(\frac{1}{N_{\text{bin}}} \sum_{i=1}^{N_{\text{bin}}} b_i\right) = \frac{1}{N_{\text{bin}}^2} \text{Var}\left(\sum_{i=1}^{N_{\text{bin}}} b_i\right) \\ &= \frac{1}{N_{\text{bin}}^2} \sum_{i,j=1}^{N_{\text{bin}}} \text{Cov}(b_i, b_j) \\ &= \frac{1}{N_{\text{bin}}^2} \left(\sum_{i=1}^{N_{\text{bin}}} \text{Var}(b_i) + 2 \sum_{1 \leq i < j \leq N_{\text{bin}}} \text{Cov}(b_i, b_j) \right), \end{aligned} \quad (\text{A1})$$

where $\text{Cov}(\cdot, \cdot)$ is the covariance. When averaging N_{bin} consecutive 15-m bins, we can consider they have approximately the
 295 same range and then that their variance is constant: $\text{Var}(b_i) = \text{Var}(b)$. If the b_i bins were uncorrelated, then we would have



$\text{Cov}(b_i, b_j) = 0, \forall (i \neq j)$, and then $\text{Var}(B) = \frac{\text{Var}(b)}{N_{\text{bin}}}$. However, since each bin is partially correlated with its vertical neighbors, we have $\text{Cov}(b_i, b_{i+m}) = \text{constant} \forall i$ for each lag of m range bins. Then, Eq. (A1) can be rewritten following

$$\begin{aligned} \text{Var}(B) &= \frac{\text{Var}(b)}{N_{\text{bin}}} \left(1 + \frac{2}{N_{\text{bin}}} \sum_{1 \leq i < j \leq N_{\text{bin}}} \frac{\text{Cov}(b_i, b_j)}{\text{Var}(b)} \right) \\ &= \frac{\text{Var}(b)}{N_{\text{bin}}} \left(1 + 2 \sum_{m=1}^{N_{\text{bin}}-1} \frac{N_{\text{bin}}-m}{N_{\text{bin}}} R(m) \right), \end{aligned} \quad (\text{A2})$$

where $R(m) = \frac{\text{Cov}(b_i, b_{i+m})}{\text{Var}(b)}$ is the autocorrelation coefficient for a lag of m range bins. It follows that the correction function
 300 to apply on the standard deviation to take into account the vertical partial correlation due to the electronic bandwidth is

$$f_a(N_{\text{bin}}) = \left(1 + 2 \sum_{m=1}^{N_{\text{bin}}-1} \frac{N_{\text{bin}}-m}{N_{\text{bin}}} R(m) \right)^{1/2}. \quad (\text{A3})$$

A2 Correction due to redistribution in altitude registration

The altitude for each sample of a raw data profile is recalculated with more accurate information about the satellite altitude and laser viewing angle in the data processing on ground. In general, shift for a few range bins is needed for the full resolution
 305 (30 m) samples. Redistribution and rebinning of two neighboring samples whose range resolutions are coarse (60 m, 180 m, and 300 m) are performed, which can induce additional correlation to the redistributed samples that also needs to be taken into account when determining the detection threshold. When there is a shift of $N_{\text{shift}15}$ 15-m bins, each new shifted bin B'_k is computed from the weighted average of the two original bins (with N_{bin} size resolution) it steps across B_k and B_{k+1} (Fig. A1) following

$$310 \quad B'_k = \frac{N_{\text{bin}} - N_{\text{shift}15}}{N_{\text{bin}}} B_k + \frac{N_{\text{shift}15}}{N_{\text{bin}}} B_{k+1}, \quad (\text{A4})$$

where

$$B_k = \frac{b_1 + b_2 + \dots + b_{N_{\text{bin}}}}{N_{\text{bin}}} = \frac{1}{N_{\text{bin}}} \sum_{i=1}^{N_{\text{bin}}} b_i, \quad (\text{A5})$$

and

$$B_{k+1} = \frac{b_{N_{\text{bin}}+1} + b_{N_{\text{bin}}+2} + \dots + b_{N_{\text{bin}}+N_{\text{bin}}}}{N_{\text{bin}}} = \frac{1}{N_{\text{bin}}} \sum_{j=1}^{N_{\text{bin}}} b_{N_{\text{bin}}+j}. \quad (\text{A6})$$



315 The variance of a B'_k can be written

$$\begin{aligned}
 \text{Var}(B'_k) &= \text{Var}\left(\frac{N_{\text{bin}} - N_{\text{shift15}}}{N_{\text{bin}}} B_k + \frac{N_{\text{shift15}}}{N_{\text{bin}}} B_{k+1}\right) \\
 &= \left(\frac{N_{\text{bin}} - N_{\text{shift15}}}{N_{\text{bin}}}\right)^2 \text{Var}(B_k) + \left(\frac{N_{\text{shift15}}}{N_{\text{bin}}}\right)^2 \text{Var}(B_{k+1}) + 2 \frac{N_{\text{bin}} - N_{\text{shift15}}}{N_{\text{bin}}} \frac{N_{\text{shift15}}}{N_{\text{bin}}} \text{Cov}(B_k, B_{k+1}) \\
 &= \left[\left(\frac{N_{\text{bin}} - N_{\text{shift15}}}{N_{\text{bin}}}\right)^2 + \left(\frac{N_{\text{shift15}}}{N_{\text{bin}}}\right)^2\right] \frac{\text{Var}(b)}{N_{\text{bin}}} f_a(N_{\text{bin}})^2 + 2 \frac{N_{\text{bin}} - N_{\text{shift15}}}{N_{\text{bin}}} \frac{N_{\text{shift15}}}{N_{\text{bin}}} \frac{\text{Var}(b)}{N_{\text{bin}}^2} \sum_{i,j=1}^{N_{\text{bin}}} \frac{\text{Cov}(b_i, b_{N_{\text{bin}}+j})}{\text{Var}(b)} \\
 &= \frac{\text{Var}(b)}{N_{\text{bin}}} \left\{ \left[\left(\frac{N_{\text{bin}} - N_{\text{shift15}}}{N_{\text{bin}}}\right)^2 + \left(\frac{N_{\text{shift15}}}{N_{\text{bin}}}\right)^2\right] f_a(N_{\text{bin}})^2 + 2 \frac{N_{\text{bin}} - N_{\text{shift15}}}{N_{\text{bin}}} \frac{N_{\text{shift15}}}{N_{\text{bin}}} \frac{1}{N_{\text{bin}}} \sum_{i,j=1}^{N_{\text{bin}}} R(N_{\text{bin}} + j - i) \right\} \quad (\text{A7}) \\
 &= \frac{\text{Var}(b)}{N_{\text{bin}}} \left\{ \left[\left(\frac{N_{\text{bin}} - N_{\text{shift15}}}{N_{\text{bin}}}\right)^2 + \left(\frac{N_{\text{shift15}}}{N_{\text{bin}}}\right)^2\right] f_a(N_{\text{bin}})^2 \right. \\
 &\quad \left. + 2 \frac{N_{\text{bin}} - N_{\text{shift15}}}{N_{\text{bin}}} \frac{N_{\text{shift15}}}{N_{\text{bin}}} \left(\sum_{m=1}^{N_{\text{bin}}} \frac{m}{N_{\text{bin}}} R(m) + \sum_{m=1}^{N_{\text{bin}}-1} \frac{N_{\text{bin}} - m}{N_{\text{bin}}} R(N_{\text{bin}} + m) \right) \right\}.
 \end{aligned}$$

It follows that the correction function to apply on the standard deviation to take into account both the vertical partial correlation due to the electronic bandwidth and the redistribution in altitude registration is

$$\begin{aligned}
 f_{\text{corr}}(N_{\text{bin}}, N_{\text{shift15}}) &= \left\{ \left[\left(\frac{N_{\text{bin}} - N_{\text{shift15}}}{N_{\text{bin}}}\right)^2 + \left(\frac{N_{\text{shift15}}}{N_{\text{bin}}}\right)^2\right] f_a(N_{\text{bin}})^2 \right. \\
 &\quad \left. + 2 \frac{N_{\text{bin}} - N_{\text{shift15}}}{N_{\text{bin}}} \frac{N_{\text{shift15}}}{N_{\text{bin}}} \left(\sum_{m=1}^{N_{\text{bin}}} \frac{m}{N_{\text{bin}}} R(m) + \sum_{m=1}^{N_{\text{bin}}-1} \frac{N_{\text{bin}} - m}{N_{\text{bin}}} R(N_{\text{bin}} + m) \right) \right\}^{1/2}. \quad (\text{A8})
 \end{aligned}$$

320 Appendix B: Surface detection

The aim of this procedure is to detect a surface echo in the near neighborhood region of the estimated surface altitude $\widehat{z}_{\text{surf}}$ given by a digital elevation model (DEM). The width of this region will vary according to surface type. Since we are highly confident of the surface altitude over the ocean (where $\widehat{z}_{\text{surf}} = 0$), we will only search in a very narrow range of altitudes for profiles measured over the ocean. On the other hand, we are somewhat less confident of the DEM surface altitudes reported
 325 over land and even much less confident over Greenland and Antarctica, so our search regions over land will be larger. The surface echo can be very weak due to attenuation by aerosol and cloud layers above. Then, we try to detect even the weakest surface echo as long as it is substantially above background noise. This procedure is applied at single-shot resolution only. For each shot, the method is made up of the following steps:

1. Compute $\widehat{r}_{\text{surf}}$, the estimated range of the surface, from $\widehat{z}_{\text{surf}}$ and the satellite altitude z_{sat} ;
- 330 2. Compute $\Delta\beta'_b(\widehat{r}_{\text{surf}})$, the standard deviation due to background noise in the β' domain at the range $\widehat{r}_{\text{surf}}$;
3. Compute i_{surf} , the bin index of the estimated surface altitude, i.e., when $z(i_{\text{surf}})$ is closest to $\widehat{z}_{\text{surf}}$;
4. Define $i_{\text{surf}} \pm \Delta i$, the range of the surface search region according to the International Geosphere/Biosphere Programme (IGBP) classification of the surface type at the lidar footprint:



- 335 (a) If surface type is *Water* and $\widehat{z}_{\text{surf}} = 0$, then $\Delta i = 2$ ($\equiv 60$ m),
 (b) Else if surface type is *Permanent-Snow*, then $\Delta i = 17$ ($\equiv 510$ m),
 (c) Else, $\Delta i = 5$ ($\equiv 150$ m);
5. Compute the derivatives of the lidar signal for bin index range 289–578 (8.2 to -0.5 km)
- $$\left(\frac{d\beta'}{dz}\right)_i = \frac{\beta'_i - \beta'_{i-1}}{z_i - z_{i-1}}; \quad (\text{B1})$$
- 340 6. Determine z_{min} and z_{max} , the altitudes of the minimum and maximum values of the derivatives in the surface search region, and i_{min} and i_{max} , their respective bin index;
7. Determine β'_{max} , the maximum signal magnitude lying between z_{min} and z_{max} ²;
8. Sequentially test the three following rules to determine if we have identified a legitimate surface return:
- (a) $z_{\text{min}} > z_{\text{max}}$,
- (b) $i_{\text{min}} - i_{\text{max}} \leq N$ with $N = 2$ for the 532 nm channels and $N = 4$ for the 1064 nm channel,
- 345 (c) $\beta'_{\text{max}} > 3\Delta\beta'_b(\widehat{r}_{\text{surf}})$;
9. If all rules passed, set surface bin index i_{surf} following these conditions:
- (a) if $\left(\frac{d\beta'}{dz}\right)_{i_{\text{min}}-1} > 0$ **or** $\beta'_{i_{\text{min}}-1} \leq 0$, then $i_{\text{surf}} = i_{\text{min}}$,
- (b) else (i.e., $\left(\frac{d\beta'}{dz}\right)_{i_{\text{min}}-1} \leq 0$ **and** $\beta'_{i_{\text{min}}-1} > 0$), $i_{\text{surf}} = i_{\text{min}} - 1$ for the 532 nm channels and $i_{\text{surf}} = i_{\text{min}} - 2$ for the 1064 nm channel.
- 350 10. If surface detection for profile k is such that $i_{\text{surf}} \notin \widehat{i}_{\text{surf}} \pm 1$ and no detection arose for profile $k - 1$ and $k + 1$, then cancel the detection of profile k .

Author contributions. TVG led the design of 2D-McDA and wrote the manuscript. MV and DW provide the knowledge of the weaknesses of the previous detection algorithm and bring the main ideas to address them. ZL developed the correction function and contributed to discussion and feedback essential to the study.

355 *Competing interests.* The authors declare that they have no conflict of interest.

²At 1064 nm, each value is repeated twice due to averaging. β'_{max} is then consider as the smallest bin index (highest altitude) of both.



Acknowledgements. The authors are grateful to Brian Magill for helping improving the runtime of the algorithm and to Kenneth Beaumont and Brian Getzewich for running the algorithm on the cluster of the Atmospheric Science Data Center. Thibault Vaillant de Guéllis' research was supported by an appointment to the NASA Postdoctoral Program at the NASA Langley Research Center, administered by Universities Space Research Association under contract with NASA.



360 References

- Bony, S., Stevens, B., Coppin, D., Becker, T., Reed, K. A., Voigt, A., and Medeiros, B.: Thermodynamic control of anvil cloud amount, *Proc. Natl. Acad. Sci. U. S. A.*, 113, 8927–8932, <https://doi.org/10.1073/pnas.1601472113>, 2016.
- Brooks, I. M.: Finding Boundary Layer Top: Application of a Wavelet Covariance Transform to Lidar Backscatter Profiles, *J. Atmos. Ocean. Tech.*, 20, 1092–1105, [https://doi.org/10.1175/1520-0426\(2003\)020<1092:FBLTAO>2.0.CO;2](https://doi.org/10.1175/1520-0426(2003)020<1092:FBLTAO>2.0.CO;2), 2003.
- 365 Campbell, J. R., Sassen, K., and Welton, E. J.: Elevated Cloud and Aerosol Layer Retrievals from Micropulse Lidar Signal Profiles, *J. Atmos. Ocean. Tech.*, 25, 685–700, <https://doi.org/10.1175/2007JTECHA1034.1>, 2008.
- Christopher, S. A., Kliche, D. V., Chou, J., and Welch, R. M.: First estimates of the radiative forcing of aerosols generated from biomass burning using satellite data, *J. Geophys. Res.- Atmos.*, 101, 21 265–21 273, <https://doi.org/10.1029/96JD02161>, 1996.
- Clothiaux, E. E., Mace, G. G., Ackerman, T. P., Kane, T. J., Spinhirne, J. D., and Scott, V. S.: An Automated Algorithm for De-
370 tection of Hydrometeor Returns in Micropulse Lidar Data, *J. Atmos. Ocean. Tech.*, 15, 1035–1042, [https://doi.org/10.1175/1520-0426\(1998\)015<1035:AAAFDO>2.0.CO;2](https://doi.org/10.1175/1520-0426(1998)015<1035:AAAFDO>2.0.CO;2), 1998.
- Davis, K. J., Gamage, N., Hagelberg, C. R., Kiemle, C., Lenschow, D. H., and Sullivan, P. P.: An Objective Method for Deriving Atmospheric Structure from Airborne Lidar Observations, *J. Atmos. Ocean. Tech.*, 17, 1455–1468, [https://doi.org/10.1175/1520-0426\(2000\)017<1455:AOMFDA>2.0.CO;2](https://doi.org/10.1175/1520-0426(2000)017<1455:AOMFDA>2.0.CO;2), 2000.
- 375 Hagihara, Y., Okamoto, H., and Yoshida, R.: Development of a combined CloudSat-CALIPSO cloud mask to show global cloud distribution, *J. Geophys. Res.-Atmos.*, 115, <https://doi.org/10.1029/2009JD012344>, 2010.
- Hartmann, D. L.: Tropical anvil clouds and climate sensitivity, *Proc. Natl. Acad. Sci. U. S. A.*, 113, 8897–8899, <https://doi.org/10.1073/pnas.1610455113>, 2016.
- Hartmann, D. L., Holton, J. R., and Fu, Q.: The heat balance of the tropical tropopause, cirrus, and stratospheric dehydration, *Geophys. Res. Lett.*, 28, 1969–1972, <https://doi.org/10.1029/2000GL012833>, 2001.
- 380 Herzfeld, U. C., McDonald, B. W., Wallin, B. F., Neumann, T. A., Markus, T., Brenner, A., and Field, C.: Algorithm for Detection of Ground and Canopy Cover in Micropulse Photon-Counting Lidar Altimeter Data in Preparation for the ICESat-2 Mission, *IEEE T. Geosci. Remote*, 52, 2109–2125, <https://doi.org/10.1109/TGRS.2013.2258350>, 2014.
- Hostetler, C. A., Liu, Z., Reagan, J., Vaughan, M., Winker, D., Osborn, M., Hunt, W. H., Powell, K. A., and Trepte, C.: Lidar Level I ATBD.
385 Calibration and Level 1 Data Products, Tech. rep., 2006.
- Huang, J., Fu, Q., Su, J., Tang, Q., Minnis, P., Hu, Y., Yi, Y., and Zhao, Q.: Taklimakan dust aerosol radiative heating derived from CALIPSO observations using the Fu-Liou radiation model with CERES constraints, *Atmos. Chem. Phys.*, 9, 4011–4021, <https://doi.org/https://doi.org/10.5194/acp-9-4011-2009>, 2009.
- Hunt, W. H., Winker, D. M., Vaughan, M. A., Powell, K. A., Lucker, P. L., and Weimer, C.: CALIPSO Lidar Description and Performance
390 Assessment, *J. Atmos. Ocean. Tech.*, 26, 1214–1228, <https://doi.org/https://doi.org/10.1175/2009JTECHA1223.1>, 2009.
- Jensen, E. J., Toon, O. B., Pfister, L., and Selkirk, H. B.: Dehydration of the upper troposphere and lower stratosphere by subvisible cirrus clouds near the tropical tropopause, *Geophys. Res. Lett.*, 23, 825–828, <https://doi.org/10.1029/96GL00722>, 1996.
- Kaufman, Y. J. and Fraser, R. S.: The effect of smoke particles on clouds and climate forcing, *Science*, 277, 1636–1639, <https://doi.org/10.1126/science.277.5332.1636>, 1997.
- 395 Lewis, J. R., Campbell, J. R., Welton, E. J., Stewart, S. A., and Haftings, P. C.: Overview of MPLNET Version 3 Cloud Detection, *J. Atmos. Ocean. Tech.*, 33, 2113–2134, <https://doi.org/10.1175/JTECH-D-15-0190.1>, 2016.



- Liu, Z. and Sugimoto, N.: Simulation study for cloud detection with space lidars by use of analog detection photomultiplier tubes, *Appl. Opt.*, 41, 1750–1759, <https://doi.org/10.1364/AO.41.001750>, 2002.
- 400 Liu, Z., Hunt, W., Vaughan, M., Hostetler, C., McGill, M., Powell, K., Winker, D., and Hu, Y.: Estimating random errors due to shot noise in backscatter lidar observations, *Appl. Opt.*, 45, 4437–4447, <https://doi.org/10.1364/AO.45.004437>, 2006.
- Lu, X., Hu, Y., Liu, Z., Rodier, S., Vaughan, M., Lucker, P., Trepte, C., and Pelon, J.: Observations of Arctic snow and sea ice cover from CALIOP lidar measurements, *Remote Sens. Environ.*, 194, 248–263, <https://doi.org/10.1016/j.rse.2017.03.046>, 2017.
- 405 Luo, B. P., Peter, T., Fueglistaler, S., Wernli, H., Wirth, M., Kiemle, C., Flentje, H., Yushkov, V. A., Khattatov, V., and Rudakov, V.: Dehydration potential of ultrathin clouds at the tropical tropopause, *Geophys. Res. Lett.*, 30, 1557, <https://doi.org/10.1029/2002GL016737>, 2003.
- McFarquhar, G. M., Heymsfield, A. J., Spinhirne, J., and Hart, B.: Thin and subvisual tropopause tropical cirrus: Observations and radiative impacts, *J. Atmos. Sci.*, 57, 1841–1853, [https://doi.org/10.1175/1520-0469\(2000\)057<1841:TASTTC>2.0.CO;2](https://doi.org/10.1175/1520-0469(2000)057<1841:TASTTC>2.0.CO;2), 2000.
- Pal, S. R., Steinbrecht, W., and Carswell, A. I.: Automated method for lidar determination of cloud-base height and vertical extent, *Appl. Opt.*, 31, 1488–1494, <https://doi.org/10.1364/AO.31.001488>, 1992.
- 410 Penner, J. E., Dickinson, R. E., and O’Neill, C. A.: Effects of aerosol from biomass burning on the global radiation budget, *Science*, 256, 1432–1434, <https://doi.org/10.1126/science.256.5062.1432>, 1992.
- Shonk, J. K. P. and Hogan, R. J.: Effect of improving representation of horizontal and vertical cloud structure on the Earth’s global radiation budget. Part II: The global effects, *Q. J. Roy. Meteor. Soc.*, 136, 1205–1215, <https://doi.org/10.1002/qj.646>, 2010.
- 415 Tsushima, Y., Emori, S., Ogura, T., Kimoto, M., Webb, M. J., Williams, K. D., Ringer, M. A., Soden, B. J., Li, B., and Andronova, N.: Importance of the mixed-phase cloud distribution in the control climate for assessing the response of clouds to carbon dioxide increase: a multi-model study, *Clim. Dynam.*, 27, 113–126, 2006.
- Vaillant de Guélis, T., Chepfer, H., Noel, V., Guzman, R., Dubuisson, P., Winker, D. M., and Kato, S.: The link between outgoing longwave radiation and the altitude at which a spaceborne lidar beam is fully attenuated, *Atmos. Meas. Tech.*, 10, 4659–4685, <https://doi.org/10.5194/amt-10-4659-2017>, 2017a.
- 420 Vaillant de Guélis, T., Chepfer, H., Noel, V., Guzman, R., Winker, D. M., and Plougonven, R.: Using Space Lidar Observations to Decompose Longwave Cloud Radiative Effect Variations Over the Last Decade: Space lidar decomposes LWCRE variations, *Geophys. Res. Lett.*, 44, 11,994–12,003, <https://doi.org/10.1002/2017GL074628>, 2017b.
- Vaillant de Guélis, T., Chepfer, H., Guzman, R., Bonazzola, M., Winker, D. M., and Noel, V.: Space lidar observations constrain longwave cloud feedback, *Sci. Rep.-UK*, 8, 16 570, <https://doi.org/10.1038/s41598-018-34943-1>, 2018.
- 425 van Zadelhoff, G.-J., Donovan, D. P., and Berthier, S.: ATLID Algorithms and Level 2 System Aspects: ATBD for A-FeatureMask, Tech. rep., 2011.
- Vaughan, M. A., Winker, D. M., and Powell, K. A.: Lidar Level II ATBD. Part 2: Feature Detection and Layer Properties Algorithms, Tech. rep., 2005.
- 430 Vaughan, M. A., Powell, K. A., Winker, D. M., Hostetler, C. A., Kuehn, R. E., Hunt, W. H., Getzewich, B. J., Young, S. A., Liu, Z., and McGill, M. J.: Fully Automated Detection of Cloud and Aerosol Layers in the CALIPSO Lidar Measurements, *J. Atmos. Ocean. Tech.*, 26, 2034–2050, <https://doi.org/10.1175/2009JTECHA1228.1>, 2009.
- Vaughan, M. A., Lee, K.-P., Garnier, A., Vaillant de Guélis, T., Getzewich, B. J., and Pelon, J.: Surface detection algorithm for space-based lidars, *Atmos. Meas. Tech.*, in progress.



- 435 Wang, Z. and Sassen, K.: Cloud Type and Macrophysical Property Retrieval Using Multiple Remote Sensors, *J. Appl. Meteorol.*, 40, 1665–1682, [https://doi.org/10.1175/1520-0450\(2001\)040<1665:CTAMPR>2.0.CO;2](https://doi.org/10.1175/1520-0450(2001)040<1665:CTAMPR>2.0.CO;2), 2001.
- Winker, D. M. and Vaughan, M. A.: Vertical distribution of clouds over Hampton, Virginia observed by lidar under the ECLIPS and FIRE ETO programs, *Atmos. Res.*, 34, 117–133, [https://doi.org/10.1016/0169-8095\(94\)90084-1](https://doi.org/10.1016/0169-8095(94)90084-1), 1994.
- 440 Winker, D. M., Pelon, J., Coakley, J. A., Ackerman, S. A., Charlson, R. J., Colarco, P. R., Flamant, P., Fu, Q., Hoff, R. M., Kittaka, C., Kubar, T. L., Le Treut, H., McCormick, M. P., Mégie, G., Poole, L., Powell, K., Trepte, C., Vaughan, M. A., and Wielicki, B. A.: The CALIPSO Mission: A Global 3D View of Aerosols and Clouds, *Bull. Amer. Meteor. Soc.*, 91, 1211–1229, <https://doi.org/10.1175/2010BAMS3009.1>, 2010.

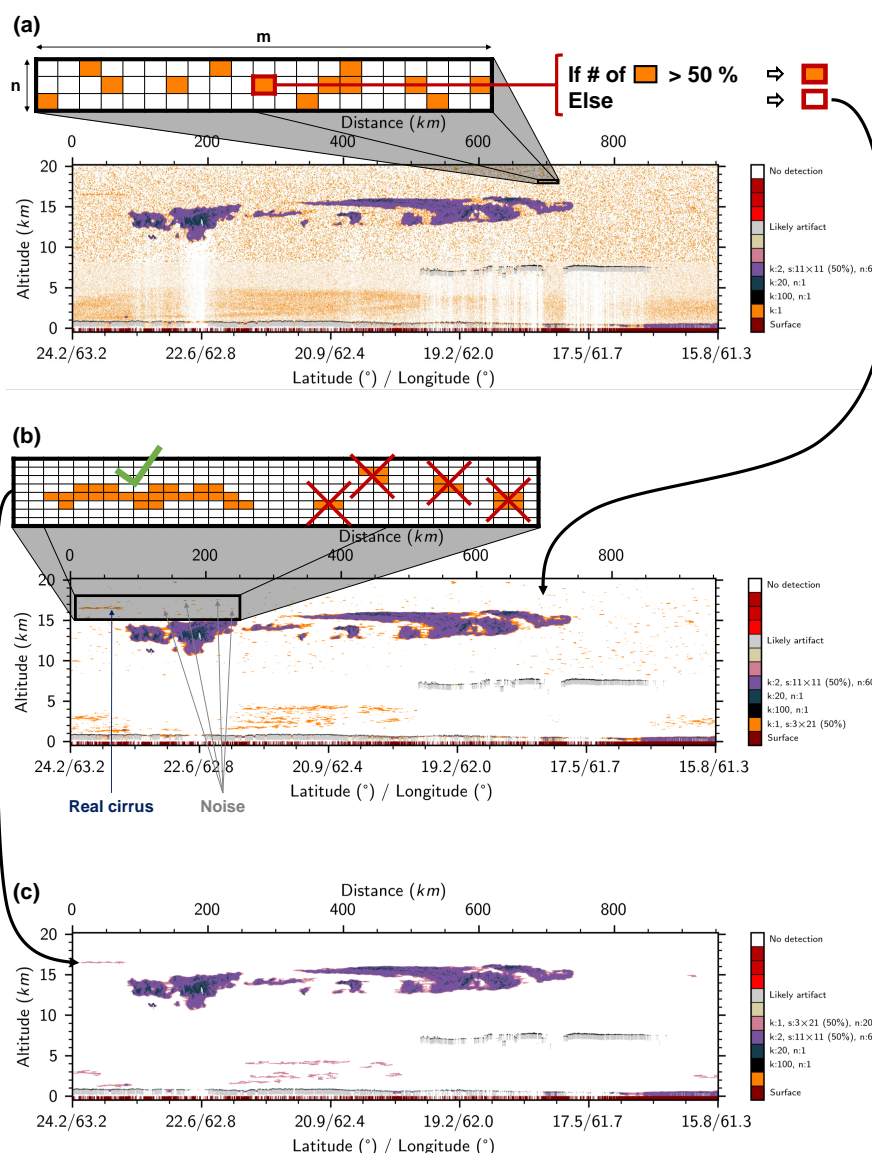


Figure 6. Illustration of the horizontal spatial coherence test window substep and the pattern size threshold rejection substep of 2D-McDA on the 532 nm parallel channel for the case study shown in Fig. 1. (a) Pixels which are over the detection threshold given by Eq. (6) with the value of $k = 1$ (orange). (b) Result after applying a 3×21 spatial coherence test window on the detected pixels. (c) Result after rejecting all patterns composed by less than $n = 200$ pixels (note that the insert on the top is just an illustration and does show the real content of the image portion). Before these substeps, surface is first detected (brown), then very strong signal ($k = 100$) occurring on highly reflecting liquid clouds is detected (black) and the 600 m below is flagged as "likely artifact" (gray) as it is the region where we see artifacts due to the time response of photomultiplier tubes (PMTs) in the 532 nm channels. Two detections were also made: one with $k = 20$ and another with $k = 2$, a 11×11 spatial coherence test window, and $n = 60$.

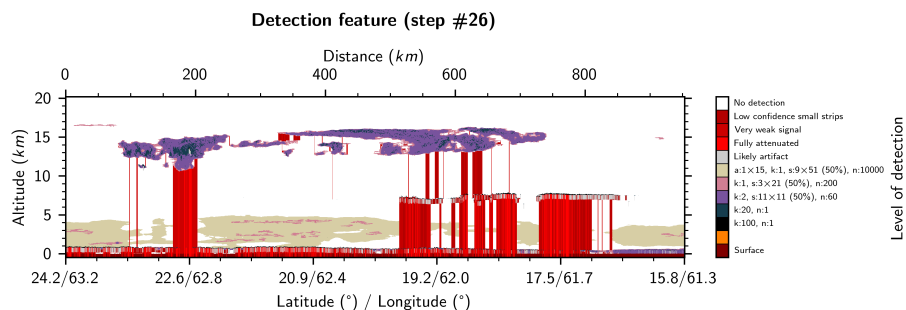


Figure 7. Final feature mask of the 532 nm parallel channel.

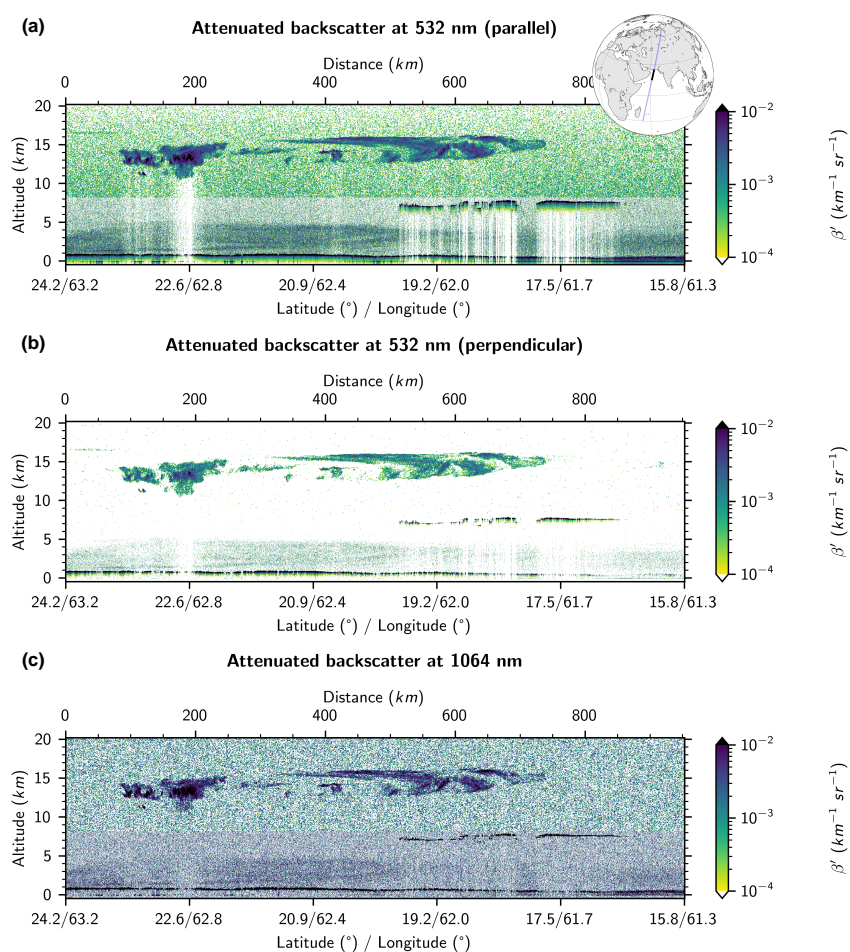


Figure 8. Curtain of lidar attenuated scattering ratio signal measured by CALIOP during nighttime observations on August 31, 21:46:37 UTC (start point), daytime observations: (a) at 532 nm parallel (same as Fig. 1), (b) at 532 nm perpendicular, and (c) 1064 nm.

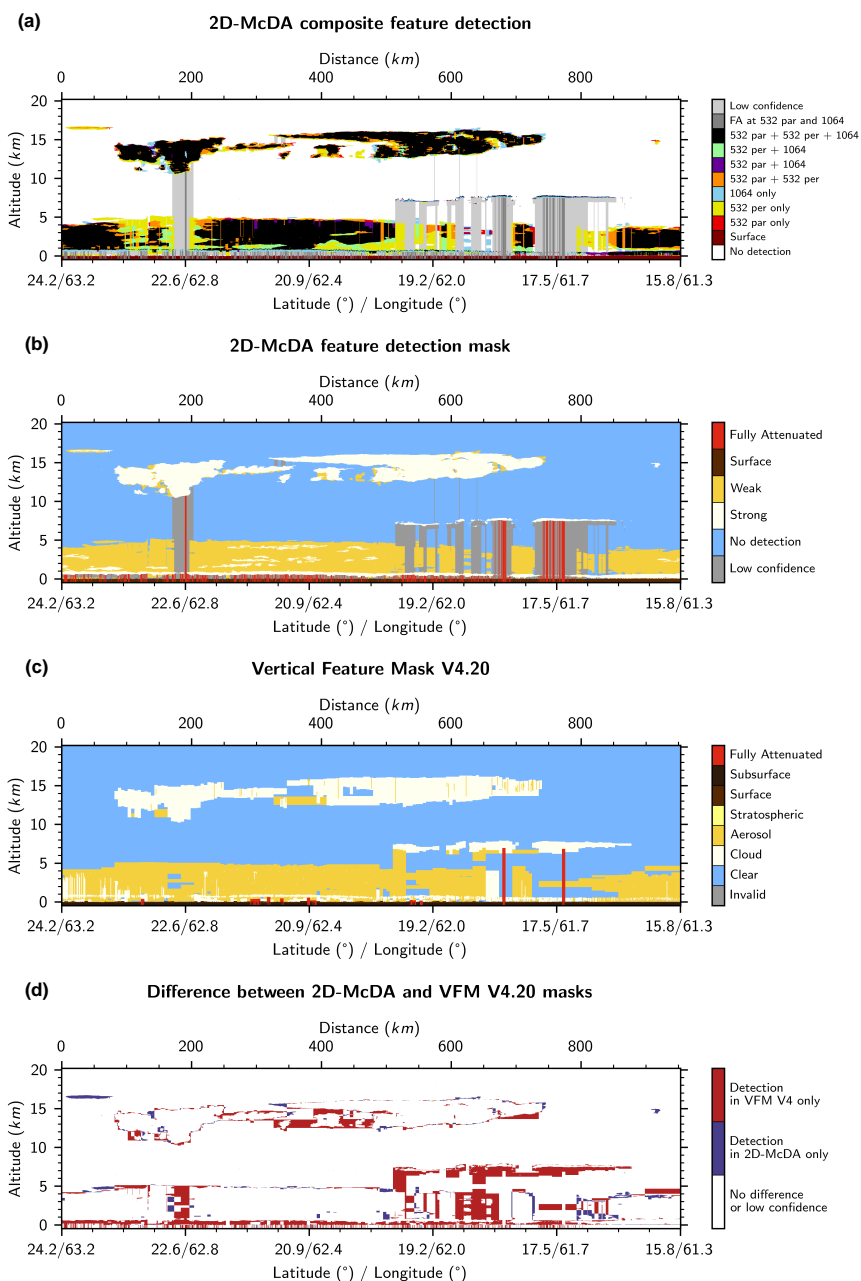


Figure 9. (a) Composite feature detection mask derived from signals shown in Fig. 8. (b) Same as (a) but using same colors than those used for VFM. "Strong" (white) are feature detected without averaging in at least one channel, others are flagged "Weak" (yellow). (c) VFM of the version 4 of the CALIOP data product. (d) Difference between new mask and VFM.

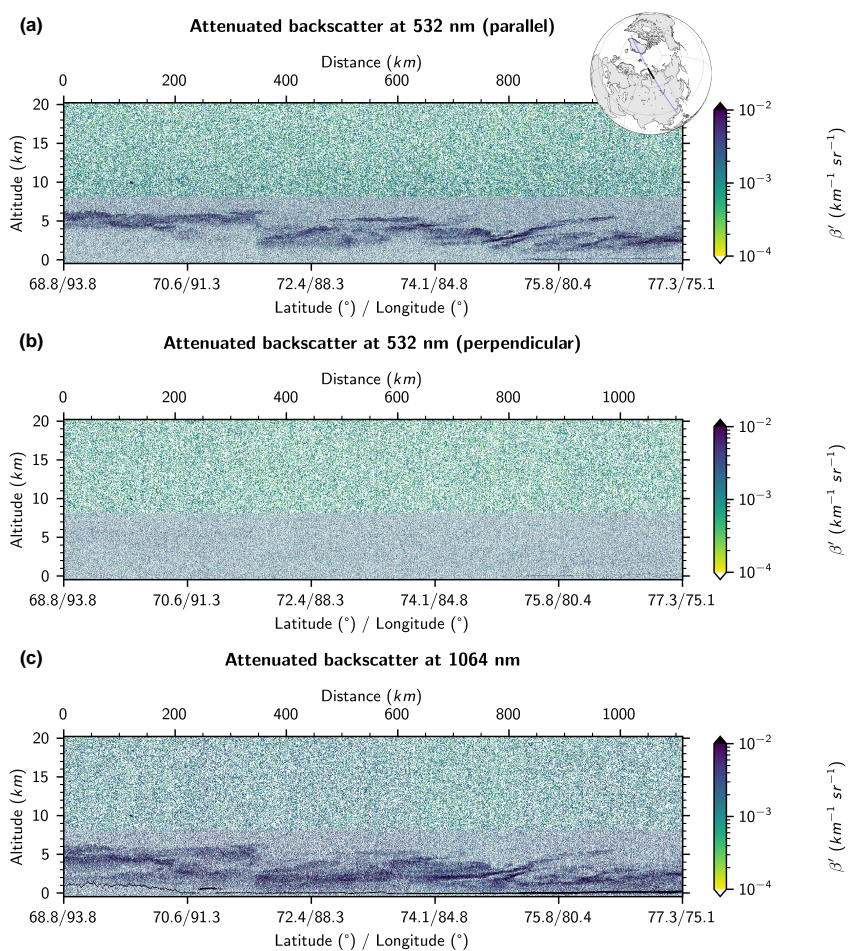


Figure 10. Curtain of lidar attenuated scattering ratio signal measured by CALIOP during a dense smoke event which occurred in Siberia on July 26, 2006, 06:00:25 UTC (start point), daytime observations: (a) at 532 nm parallel, (b) at 532 nm perpendicular, and (c) 1064 nm.

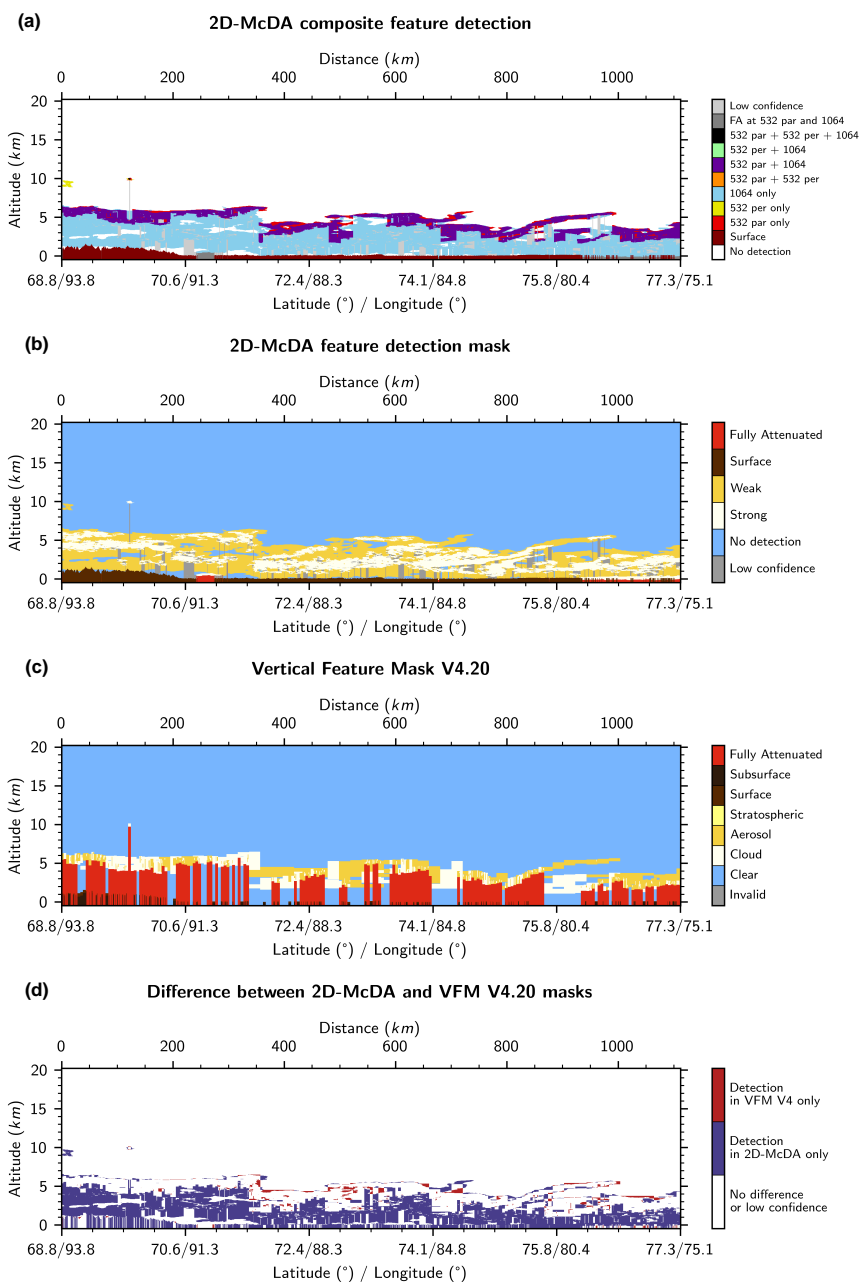


Figure 11. (a) Composite feature detection mask derived from signals shown in Fig. 10. (b) Same as (a) but using same colors than those used for VFM. "Strong" (white) are feature detected without averaging in at least one channel, others are flagged "Weak" (yellow). (c) VFM of the version 4 of the CALIOP data product. (d) Difference between new mask and VFM.

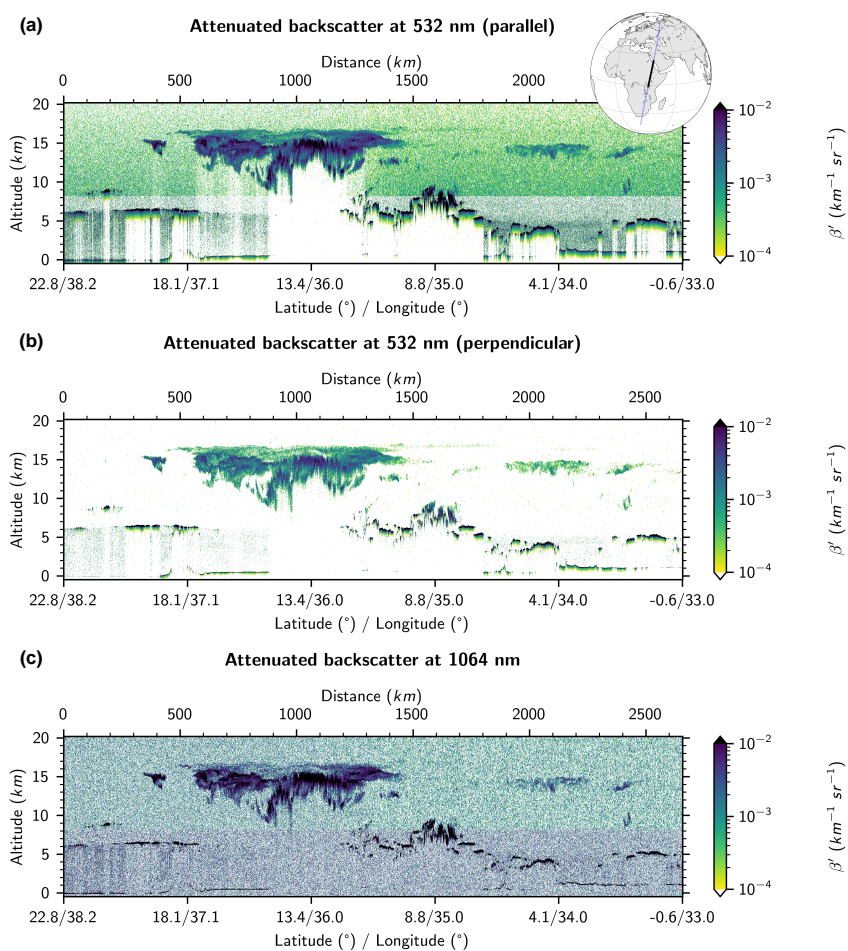


Figure 12. Curtain of lidar attenuated scattering ratio signal measured by CALIOP during nighttime observations on August 31, 2018, 23:25:54 UTC (start point), over Ethiopia: (a) at 532 nm parallel, (b) at 532 nm perpendicular, and (c) 1064 nm.

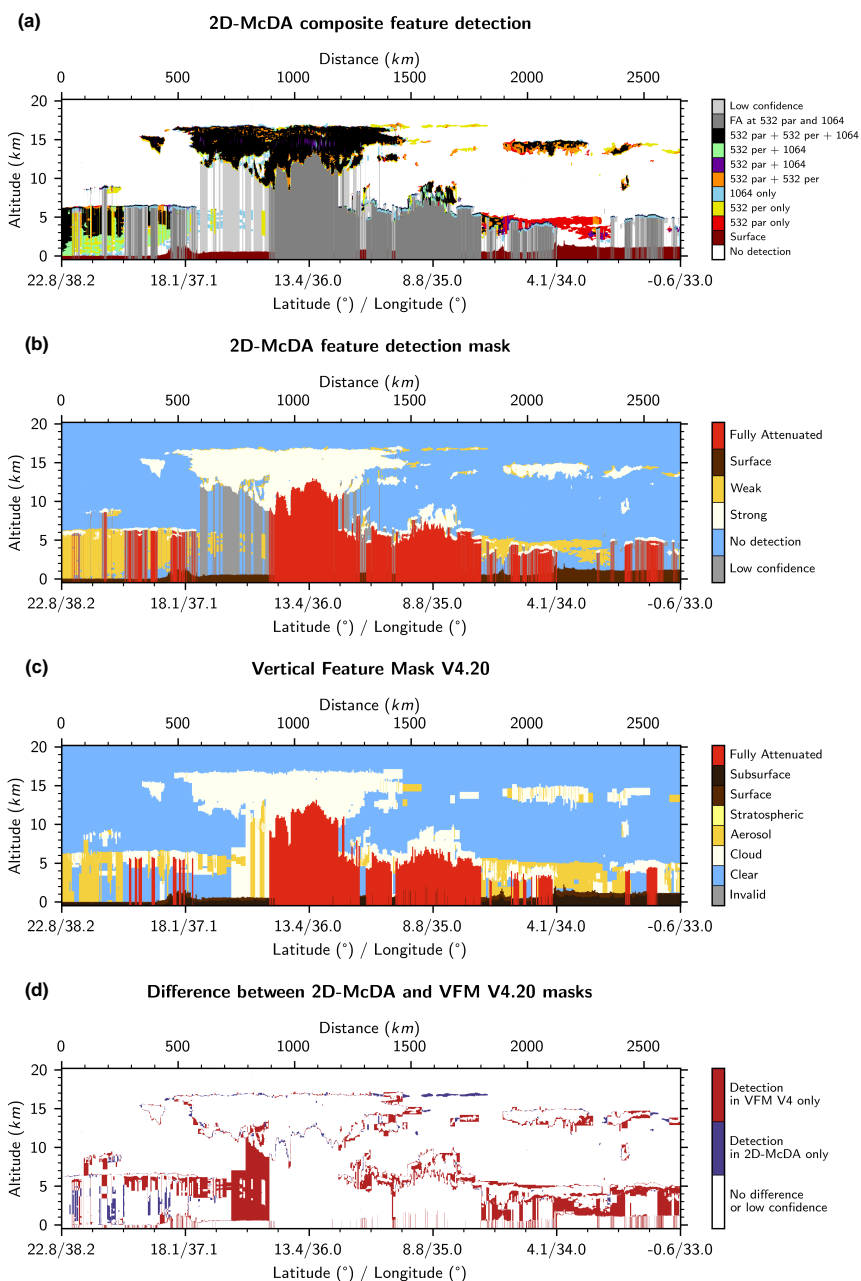


Figure 13. (a) Composite feature detection mask derived from signals shown in Fig. 12. (b) Same as (a) but using same colors than those used for VFM. "Strong" (white) are feature detected without averaging in at least one channel, others are flagged "Weak" (yellow). (c) VFM of the version 4 of the CALIOP data product. (d) Difference between new mask and VFM.

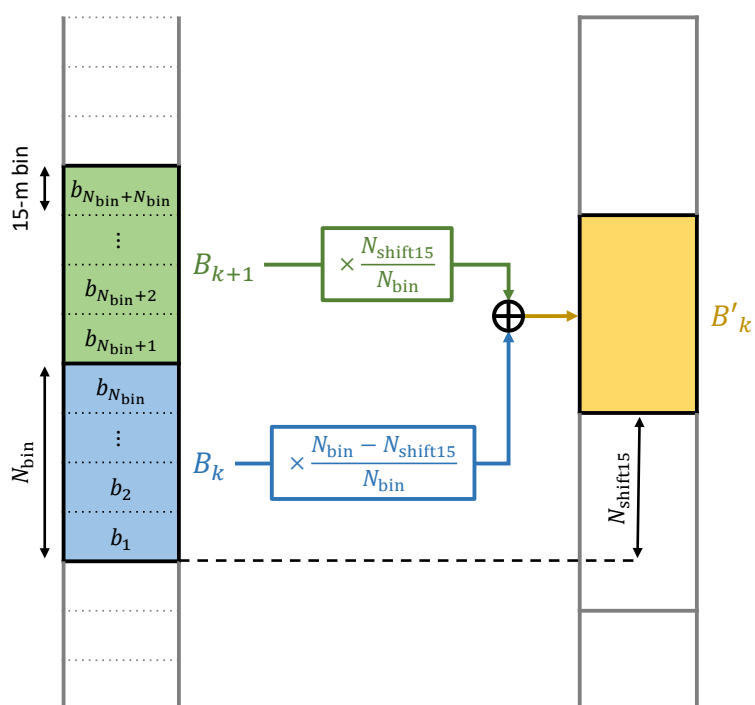


Figure A1. Scheme of redistribution in altitude registration.